

Article

Diurnal and Seasonal Variation of High-Frequency Gravity Waves at Mohe and Wuhan

Yiyun Wu ¹, Qiong Tang ², Zhou Chen ¹, Yi Liu ¹ and Chen Zhou ^{1,*} 

¹ Department of Space Physics, School of Electronic Information, Wuhan University, Wuhan 430072, China; wuyiyun@whu.edu.cn (Y.W.); zhouchen_whu@whu.edu.cn (Z.C.); liuyiwuhan@whu.edu.cn (Y.L.)

² Institute of Space Science and Applied Technology, Harbin Institute of Technology (Shenzhen), Shenzhen 518055, China; tangqiong@hit.edu.cn

* Correspondence: chenzhou@whu.edu.cn

Abstract: Using the meteor radar data at the Mohe (53.5° N, 122.3° E) and Wuhan (30.5° N, 114.2° E) regions over China, this paper conducts a study on the diurnal and seasonal variation of high-frequency (within 2 h) gravity waves (GWs) activity in the mesosphere and the lower thermosphere (MLT). On the basis of the composite day analysis and Hocking's technique, the variance and momentum flux of the high-frequency GWs are derived from the radial velocities of individual meteor trails. Spectral results demonstrate that the high-frequency GWs activity shows 12 and 24 h periodicity, which may be due to the tidal modulation on the high-frequency GWs. The spectra of the variance and momentum flux also show 6 and 8 h periodicity. In addition to the diurnal variation, the high-frequency GWs activity shows the annual and semiannual oscillations. Additionally, the quasi-4-month oscillation is found at Mohe.

Keywords: MLT region; meteor radar; gravity waves; momentum flux



Citation: Wu, Y.; Tang, Q.; Chen, Z.; Liu, Y.; Zhou, C. Diurnal and Seasonal Variation of High-Frequency Gravity Waves at Mohe and Wuhan. *Atmosphere* **2022**, *13*, 1069. <https://doi.org/10.3390/atmos13071069>

Academic Editor: Yoshihiro Tomikawa

Received: 1 June 2022

Accepted: 28 June 2022

Published: 6 July 2022

Publisher's Note: MDPI stays neutral with regard to jurisdictional claims in published maps and institutional affiliations.



Copyright: © 2022 by the authors. Licensee MDPI, Basel, Switzerland. This article is an open access article distributed under the terms and conditions of the Creative Commons Attribution (CC BY) license (<https://creativecommons.org/licenses/by/4.0/>).

1. Introduction

The mesosphere and the lower thermosphere (MLT) comprise the region from about 60 to 110 km [1]. It is the transition region between the neutral atmosphere and the ionosphere. The MLT region is strongly modulated by gravity waves (GWs), which are primarily excited by topography, convection, wind shear, jet streams and frontal systems [2]. As GWs transport up through the atmosphere, the amplitudes grow to conserve energy. GWs that reach the MLT region dissipate and/or break [3,4]. The deposition of the energy and momentum by wave breaking plays a crucial role in the dynamic and energy balance of the MLT region [5]. The effects of GWs on the MLT region include the wind deceleration in the mesosphere, which leads to the reversals of the mesopause wind, the residual mesospheric circulation from pole to pole, which leads to a cold summer and warm winter in the mesopause region and the coupling of GWs with larger-scale waves (e.g., tides and planetary waves) [6–8]. On account of the small horizontal phase speed of GWs, which is of the order of the background mean flow, GWs are very sensitive to the wind filtration in the middle atmosphere. Therefore, the amplitudes of GWs depend on both the seasonal cycle and planetary waves [9,10].

An important property of GWs is that they can transport and deposit momentum and energy from the lower atmosphere to the upper atmosphere, and the vertical flux of horizontal momentum (momentum flux for short) is used to quantify this property. Extensive studies show that the momentum flux of high-frequency GWs presents significant seasonal variation. Matsumoto et al. [11] analyzed the data of two nearly identical meteor radars at Koto Tabang (0.20° S, 100.32° E), West Sumatra, and Biak (1.17° S, 136.10° E), West Papua, and found that the seasonal variations in the momentum flux showed the semiannual and annual oscillations. Placke et al. [12] also found the periodic oscillations of the momentum flux using the data of the meteor radar wind measurements at Collm,

Germany (51.3° N, 13.0° E), and explained it by the wind filtering of GWs. In addition, Andrioli et al. [5] found for the first time that the zonal momentum flux at Santa Maria (30° S, 54° W) and the meridional momentum flux at 92.5 km over Cachoeira Paulista (23° S, 45° W) showed a quasi-4-month oscillation. Liu et al. [13] studied the diurnal variation of the momentum flux of GWs, and their results showed that the momentum flux of GWs was strongly modulated by the diurnal tide. Manson et al. [14] analyzed the data of the Saskatoon medium frequency (MF) radar (52° N, 107° W) for the years 1992 and 1993 and found that when the propagation directions of the momentum flux of GWs were isotropic, the momentum flux of GWs presented a 6 h modulation.

The horizontal wind variance caused by high-frequency GWs (period less than 2 h) is an important symbol of GWs activity. The observation investigations of the high-frequency GWs activity of the MLT region mainly focus on its seasonal variation. Based on the data of two meteor radars, one at Rothera in the Antarctic (68° S) and one at Esrange in the Arctic (68° N), Beldon and Mitchell [15] identified that the high-frequency GWs activity showed a semiannual oscillation. Andrioli et al. [5] found the annual and semiannual oscillations in seasonal variations of high-frequency GWs activity at Cariri (7° S, 36° W), Cachoeira Paulista (23° S, 45° W) and Santa Maria (30° S, 54° W). In addition, the quasi-4-month oscillation of the meridional variance of GWs is found at Mohe (53.5° N, 122.3° E), Beijing (40.3° N, 116.2° E), Mengcheng (33.3° N, 116.5° E) and Wuhan (30.5° N, 114.2° E) [16]. In addition to seasonal variations, the high-frequency GWs also present the diurnal and semidiurnal variations. Andrioli et al. [17] re-analyzed the previous data at Cariri (7° S, 36° W), Cachoeira Paulista (23° S, 45° W), Santa Maria (30° S, 54° W) and Southern Argentina Agile (53.8° S, 67.8° W) and found the diurnal and semidiurnal modulations on GWs variance over all sites. In addition, the semidiurnal modulation was observed at lower latitudes mainly near the equinoxes, while the diurnal modulation occurred mainly near the solstices.

To analyze GWs, different kinds of instruments have been used, such as radars [14], lidars [18], rocket soundings [19] and satellites such as TIMED (SABER) [20]. The meteor radars are suitable to monitor GWs at long time scales, owing to their operation being continuous, automatic and with relatively less expense. Billions of meteoroids enter the Earth's atmosphere every day, rapidly burning and ionizing their surfaces as they collide with atmospheric molecules. A long and thin column of high-density plasma left behind by a meteor is a meteor trail. By transmitting radio waves and receiving the reflection echo of the meteor trail, the meteor radar can obtain the distance from the meteor trail to the receiving point, zenith angle, azimuth angle and radial velocity, so as to calculate and invert estimate the variance and momentum flux of GWs. The all-sky meteor radar is used to observe and study the fluctuation and propagation characteristics of the global middle and upper atmosphere, the dynamics of the middle and upper atmosphere and the coupling between the middle and upper atmosphere and the ionosphere.

In this paper, we aim to investigate the diurnal and seasonal variations of high-frequency (within 2 h) GWs activity by using Mohe (53.5° N, 122.3° E) and Wuhan (30.5° N, 114.2° E) meteor radar data from 2012 to 2019. The paper is organized as follows. The meteor radar data utilized and the method used in the paper are described in Section 2. The diurnal and seasonal variations of high-frequency GWs activity at two stations are presented in Section 3. The discussion is given in Section 4, and the summary is given in Section 5.

2. Datasets and Methods

2.1. Datasets

The all-sky meteor radars use wide beam transmission, interferometry, Doppler shift and automatic identification of meteor trails [21,22], which can detect radial velocity, distance and other parameters of a meteor's trails from 70 km to 110 km [21]. Meteor radars have large vertical and temporal resolutions, typically 2 km and 1 h. The Mohe and Wuhan

meteor radar data from 2012 to 2019 are used in this paper. Figure 1 shows the geographical distribution of Mohe and Wuhan meteor radar stations.

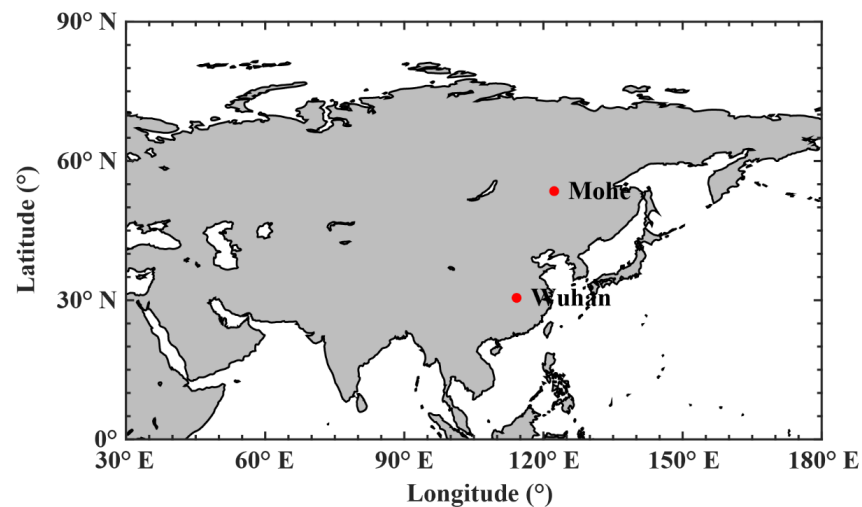


Figure 1. Geographical distribution of Mohe and Wuhan meteor radar stations.

2.2. Method

Reid and Vincent [23] first introduced the dual beam technique for momentum flux calculations. Hocking [24] generalized this formulation and used meteor radar to measure horizontal wind variance and momentum flux. Hocking [24] also applied the technique to data from mid-latitude and polar sites with an averaging interval of less than 3 h in height/time bins. The results suggested that variance and momentum flux were caused by GWs with a period of less than 2–3 h, with contamination caused by tides and planetary waves removed. Vincent et al. [25] evaluated this method and proposed that as long as there were enough meteor trails in a certain time and altitude range, the meaningful values of GWs can be obtained from the meteor radars. In recent years, based on Hocking's technique, many studies have used composite day analysis with the aim to avoid contamination by tidal and planetary waves with improved accuracy [26,27]. All meteors from the specified time and altitude range of a calendar month are aggregated into a composite day and treated as one-day meteors.

Compared to the period of GWs, each meteor echo is basically a localized wind measurement on a small atmospheric volume and a small timescale. After removing the contributions of large-scale motions to the horizontal wind velocity, such as background wind, tide, planetary waves and long-period gravitational waves, the variance of the remaining small-scale motions can be considered to be dominated by GW perturbations, so it can be used as a proxy for GWs activity [15]. Based on Hocking's technique and composite day analysis, this paper infers the variance and momentum flux of GWs using the all-sky meteor radar data.

The background wind variance caused by high-frequency GWs (period of less than 2 h) is an important indicator of GWs activity. Hocking [24] used three-hourly data bins, shifted in step of 2 h to analyze high-frequency GWs, and obtained the reliable result. To better study the high-frequency GWs, time intervals of 2 h and displacement between adjacent intervals of 1 h (centered on the hours from 00:00 to 23:00) and altitude intervals of 3 km and displacement between adjacent intervals of 3 km (centered on 78.5, 81.5, 84.5, 87.5, 90.5, 93.5 and 96.5 km) are used in this paper. Large-scale waves with a period greater than 2 h and a height scale greater than 3 km are filtered by the bins. The data in this period are relatively continuous and complete. Since meteors with small zenith angles may cause large horizontal velocity errors, and meteors with large zenith angles may cause large height measurement errors, the paper only processes and analyzes the data with zenith angles between 15° and 60° [16]. Meteors with measured radial velocities greater than 200 m/s may contain rapidly decaying meteors, so these meteor data will be removed [12].

The background mean wind velocities are calculated by the least squares fit of radial velocities. The background mean wind velocity of each bin is fitted by the Equation (1)

$$\vec{v} = \begin{bmatrix} \sum \cos^2 \theta_{xi} & \sum \cos \theta_{xi} \cos \theta_{yi} & \sum \cos \theta_{xi} \cos \theta_{zi} \\ \sum \cos \theta_{yi} \cos \theta_{xi} & \sum \cos^2 \theta_{yi} & \sum \cos \theta_{yi} \cos \theta_{zi} \\ \sum \cos \theta_{zi} \cos \theta_{xi} & \sum \cos \theta_{zi} \cos \theta_{yi} & \sum \cos^2 \theta_{zi} \end{bmatrix}^{-1} \begin{bmatrix} \sum v_{radi} \cos \theta_{xi} \\ \sum v_{radi} \cos \theta_{yi} \\ \sum v_{radi} \cos \theta_{zi} \end{bmatrix} \quad (1)$$

where θ_{xi} , θ_{yi} and θ_{zi} are the angles between each meteor trail and the axes of the space rectangular coordinate system, and v_{radi} is the radial velocity of each meteor trail. To ensure the accuracy of background horizontal wind calculation, the number of meteors in a given window in each natural day should not be less than 10 [25]. In addition, if the difference between the actual and projected radial wind velocity exceeds 25 m/s, the meteor will be removed. The least squares fit is repeated until no meteors are removed [22]. In order to correct the errors caused by vertical and temporal shears of the background wind, the bilinear interpolation is used to calculate the background mean wind corresponding to the exact time and height of each meteor trail [26]. After interpolation, meteor trails outside the heights range of 78.5–96.5 km are removed, and the height windows are repartitioned (centers on 80, 83, 86, 89, 92 and 95 km). Assuming that the disturbance radial velocities follow a Gaussian distribution, the rule of 5-standard-deviations criterion is used to eliminate outliers that are large enough to cause deviations [27].

Hocking’s technique is used to calculate the variance and momentum flux within a composite day. Make sure that there are at least 30 meteors in each window. The coordinate of each meteor trail is (θ, ϕ) in the celestial coordinate system, where θ, ϕ are the zenith and azimuth angels. The radial velocity of each meteor trail is calculated by the Equation (2)

$$v_{rad} = (\bar{u} \sin \theta \cos \phi + \bar{v} \sin \theta \sin \phi + \bar{w} \cos \theta) + (u' \sin \theta \cos \phi + v' \sin \theta \sin \phi + w' \cos \theta) \quad (2)$$

where $\bar{u}, \bar{v}, \bar{w}$ and \bar{v}_{rad} are the average zonal, meridional, vertical and radial velocities of each bin, and u', v', w' and v'_{rad} are the disturbance values caused by the GWs activity. Hocking’s technique is the least square fitting of the disturbed radial velocities, and the calculation equation is given below:

$$\begin{bmatrix} \sum \sin^4 \theta \cos^4 \phi & \sum \sin^4 \theta \sin^2 \phi \cos^2 \phi & \sum \sin^2 \theta \cos^2 \theta \cos^2 \phi & \sum 2 \sin^4 \theta \cos^3 \phi \sin \phi \\ \sum \sin^4 \theta \cos^2 \phi \sin^2 \phi & \sum \sin^4 \theta \sin^4 \phi & \sum \cos^2 \theta \sin^2 \theta \sin^2 \phi & \sum 2 \sin^4 \theta \cos \phi \sin^3 \phi \\ \sum \sin^2 \theta \cos^2 \theta \cos^2 \phi & \sum \sin^2 \theta \cos^2 \theta \sin^2 \phi & \sum \cos^4 \theta & \sum 2 \sin^2 \theta \cos^2 \theta \cos \phi \sin \phi \\ \sum \sin^4 \theta \cos^3 \phi \sin \phi & \sum \sin^4 \theta \sin^3 \phi \cos \phi & \sum \sin^2 \theta \cos^2 \theta \cos \phi \sin \phi & \sum 2 \sin^4 \theta \cos^2 \phi \sin^2 \phi \\ \sum \sin^3 \theta \cos \theta \cos^3 \phi & \sum \sin^3 \theta \cos \theta \sin^2 \phi \cos \phi & \sum \cos^3 \theta \sin \theta \cos \phi & \sum 2 \sin^3 \theta \cos \theta \cos^2 \phi \sin \phi \\ \sum \sin^3 \theta \cos \theta \cos^2 \phi \sin \phi & \sum \sin^3 \theta \cos \theta \sin^3 \phi & \sum \cos^3 \theta \sin \theta \sin \phi & \sum 2 \sin^3 \theta \cos \theta \cos^2 \phi \sin^2 \phi \end{bmatrix} \begin{bmatrix} u^2 \\ v^2 \\ w^2 \\ u'v' \\ uv' \\ v'w \end{bmatrix} = \begin{bmatrix} \sum \sin^2 \theta \cos^2 \phi (v'_{rad})^2 \\ \sum \sin^2 \theta \sin^2 \phi (v'_{rad})^2 \\ \sum \cos^2 \theta (v'_{rad})^2 \\ \sum \sin^2 \theta \cos \phi \sin \phi (v'_{rad})^2 \\ \sum \sin \theta \cos \theta \cos \phi (v'_{rad})^2 \\ \sum \sin \theta \cos \theta \sin \phi (v'_{rad})^2 \end{bmatrix} \quad (3)$$

The Lomb–Scargle (LS) spectral method is often used to analyze the variation of GWs activity [5,14,28]. To study and analyze the diurnal variations of GWs activity, LS spectral method is used in this paper to analyze the periodicity of the background horizontal wind, the horizontal variance and the momentum flux. To obtain more general results, we combine the data of the same calendar month of 2012–2019 into a day according to height and time. The LS spectral analysis of 12 composite days was carried out with the aim to analyze their diurnal variation. The height windows center on 80, 83, 86, 89, 92 and 95 km with 3 km intervals and 3 km steps, and the time window centers on the hours from 00:00 to 23:00 with 2 h intervals and 1 h steps. To analyze their seasonal variation, we

obtained 96 consecutive composite days from years 2012 to 2019 and averaged different time windows within the same heights range in the same composite day. In the process of seasonal spectral analysis, the height window remains the same, while the time window centers on 96 consecutive months with 1-month intervals and 1-month steps.

3. Results and Analysis

3.1. Diurnal Variation

Figure 2 presents the LS spectra of the background zonal wind (left column), zonal momentum flux (middle column) and zonal variance (right column) using composite day analysis for 12 calendar months at Mohe. The black solid lines indicate 95% confidence levels. As shown in the left column of Figure 2, apart from April and May, the background zonal wind at Mohe presents 24 h periodicity with confidence intervals greater than 95% at all height ranges. While in April and May, the 12 h period is only observed above 92 km height. In addition, 24 h periodicity can be seen in the height range below 89 km in April. We can see from the middle column of Figure 2 that the 12 h periodicity in zonal momentum flux of GWs can be seen in January, February, March, September, October, November and December at a certain heights range. In addition, a 24 h period in the zonal momentum flux is also observed in May, June and August. A weak 6 h period occurs in July and November. Note that the intensity of the variance represents the intensity of GWs activity. As shown in the right column of Figure 2, the zonal variance only shows a 12 h period below 83 km in August and September and a 24 h period in all months apart from February, September and December. In addition, a weak 6 h period is observed in December, and a weak 8 h period occurs in November and December.

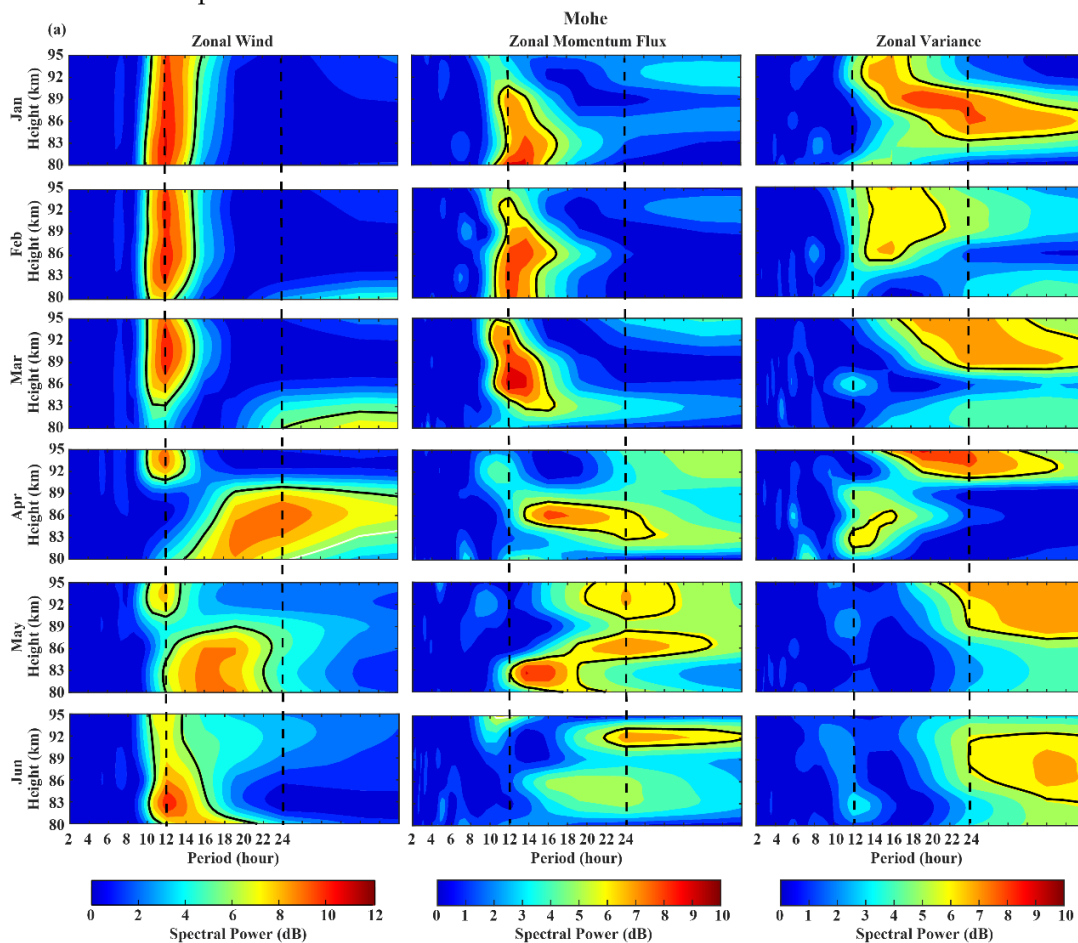


Figure 2. Cont.

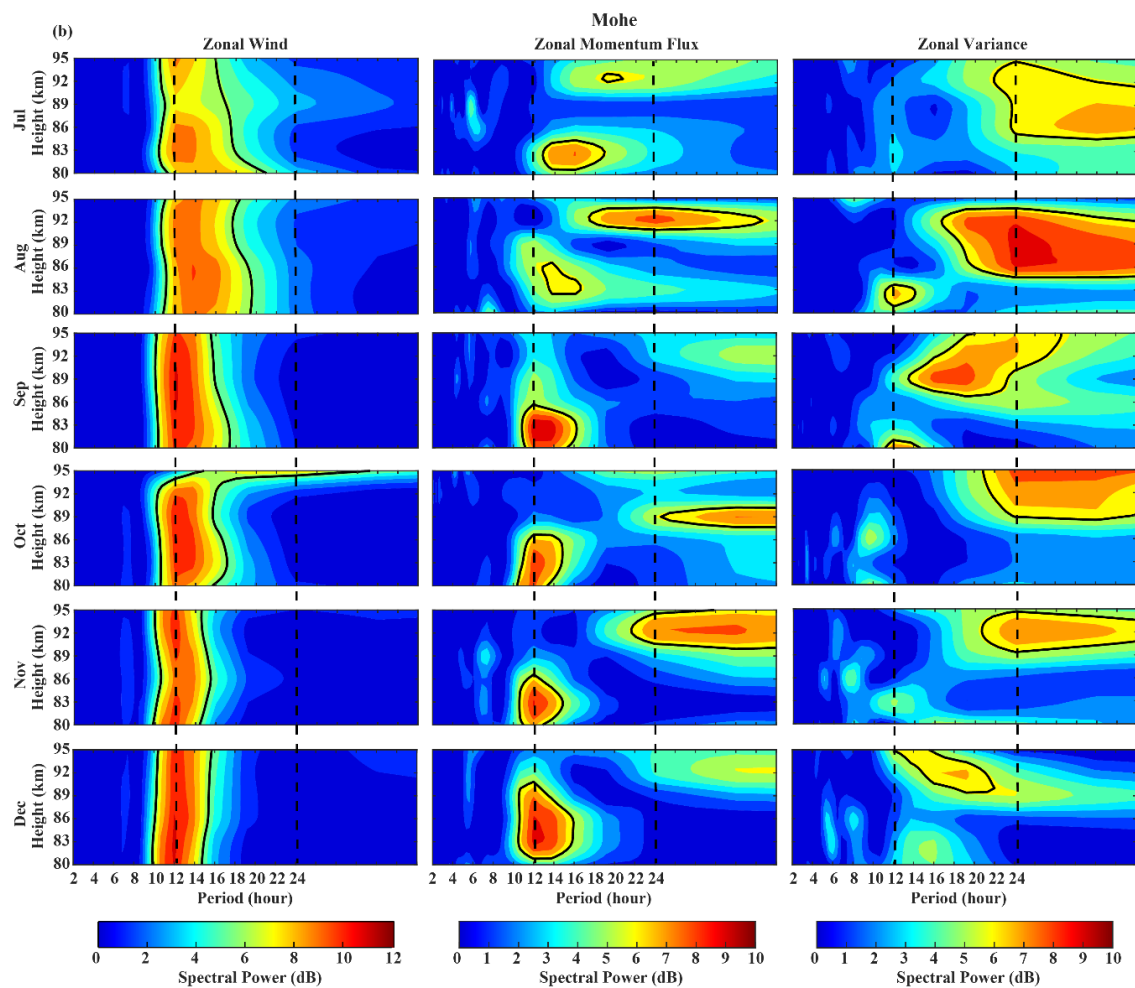


Figure 2. LS spectra of the background zonal wind (left column), zonal momentum flux (middle column) and zonal variance (right column) using composite day analysis for 12 calendar months at Mohe. The black solid lines indicate 95% confidence levels. (a) LS spectra from January to June; (b) LS spectra from July to December.

Figure 3 presents the LS spectra of the background zonal wind (left column), zonal momentum flux (middle column) and zonal variance (right column) using composite day analysis for 12 calendar months at Wuhan. The black solid lines indicate 95% confidence levels. As shown in the left column of Figure 3, the background zonal wind at Wuhan shows an obvious 24 h periodicity with confidence intervals greater than 95% in the period from February to April and from September to November. The 12 h period in the background zonal wind can be found in May and June below 83 km. It can be seen from the middle column of Figure 3 that the 12 h period in the zonal momentum flux is observed at a certain heights range in January, May, June, July, August and September. The 24 h period in the momentum flux occurs in February, March, April and November. In addition, a weak 6 h period is observed in February, April and May, and a weak 8 h modulation is also observed in April. Note that when the momentum flux shows a 24 h variation, the zonal wind also shows a strong 24 h period at the same time and height. As shown in the right column of Figure 3, the zonal variance presents an obvious 24 h variation at a certain heights range in all months apart from September, November and December. The 12 h period is also obvious in February, March, April and October below 86 km.

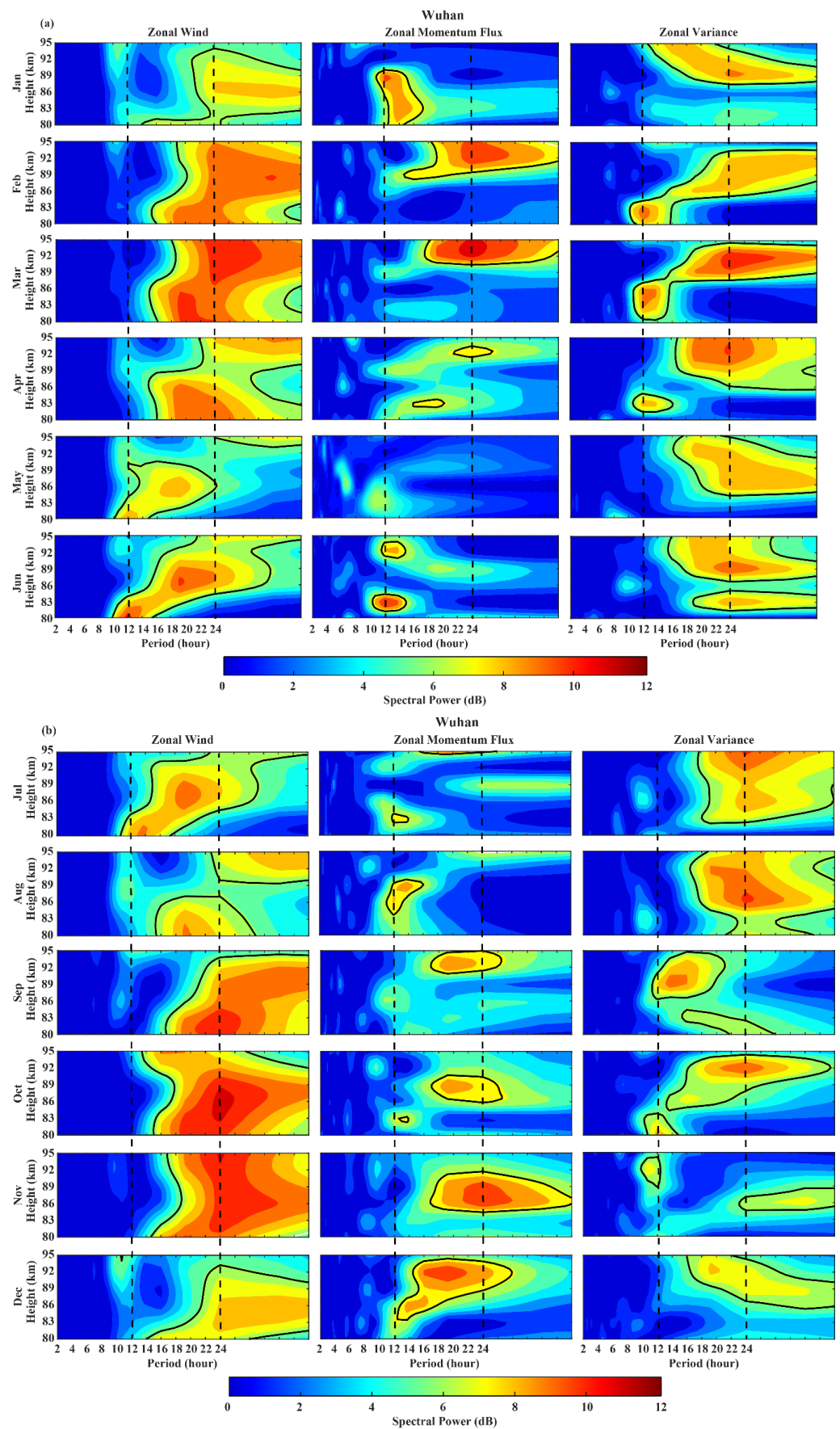


Figure 3. LS spectra of the background zonal wind (left column), zonal momentum flux (middle

column) and zonal variance (right column) using composite day analysis for 12 calendar months at Wuhan. The black solid lines indicate 95% confidence levels. (a) LS spectra from January to June; (b) LS spectra from July to December.

Figure 4 presents the LS spectra of the background meridional wind (left column), meridional momentum flux (middle column) and meridional variance (right column) using composite day analysis for 12 calendar months at Mohe. The black solid lines indicate 95% confidence levels. Similar to the background zonal wind, it can be seen from the left column of Figure 4 that the background meridional wind at Mohe also shows an obvious 12 h period almost at all heights ranges in all months apart from April. As shown in the middle column of Figure 4, the meridional momentum flux presents a 24 h periodicity in April and May and the 12 h periodicity during the time period from August to October. In addition, an 8 h period with confidence intervals greater than 95% is observed in September, while a weak 6 h period is observed in February. It can be seen from the right column of Figure 4 that the meridional variance presents a 24 h period at a certain heights range in January, February, March, April and October. A 12 h period can be found in June, July, October and November. In addition, a weak 8 h period can be seen in May and September.

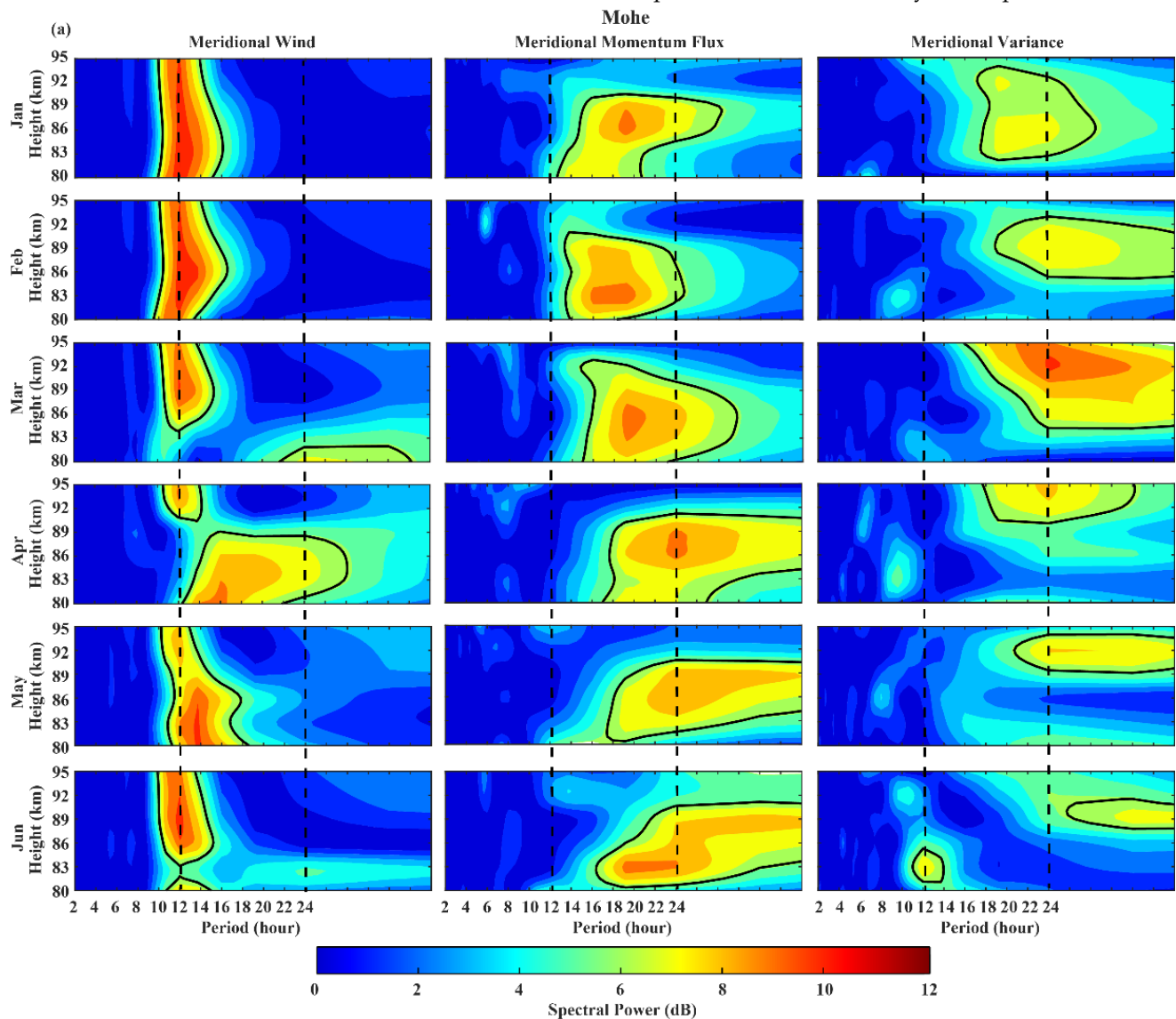


Figure 4. Cont.

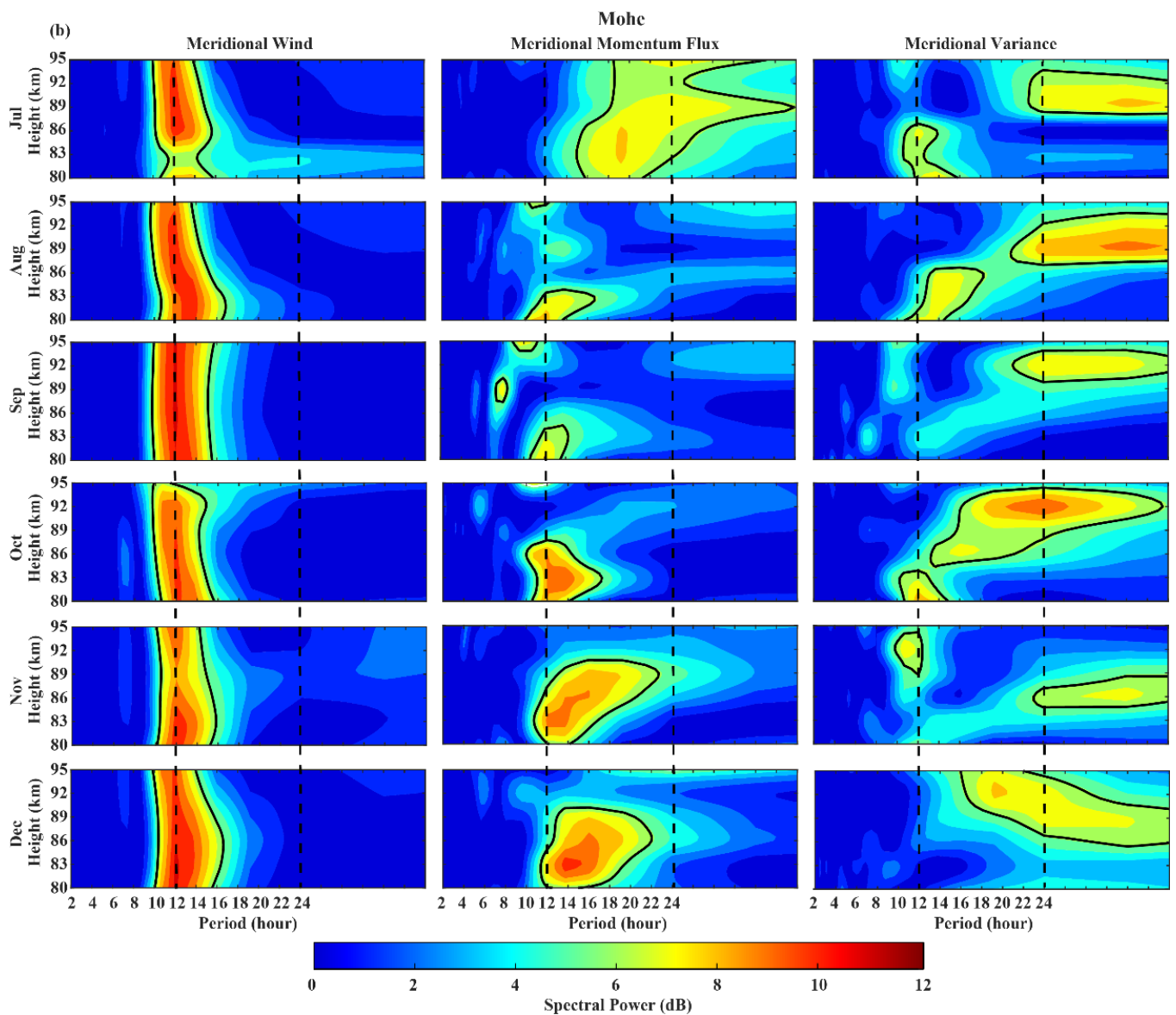


Figure 4. LS spectra of the background meridional wind (left column), meridional momentum flux (middle column) and meridional variance (right column) using composite day analysis for 12 calendar months at Mohe. The black solid lines indicate 95% confidence levels. (a) LS spectra from January to June; (b) LS spectra from July to December.

Figure 5 presents the LS spectra of the background meridional wind (left column), meridional momentum flux (middle column) and meridional variance (right column) using composite day analysis for 12 calendar months at Wuhan. The black solid lines indicate 95% confidence levels. Similar to the zonal wind, the meridional wind at Wuhan also presents an obvious 24 h periodicity at a certain heights range in all months apart from May, June and July. A 12 h period occurs below 86 km in May and June. As shown in the middle column of Figure 5, the meridional momentum flux also shows the 24 h periodicity at a certain heights range in all months apart from June, August, September, October and December. In addition, the 12 h period occurs in September, October and November. An 8 h period is observed in February, March, July, August, September and October. It can be seen from the right column of Figure 5 that the meridional variance presents 24 h periodicity in all months apart from February, March, October and November. The 12 h period can be seen in March and October.

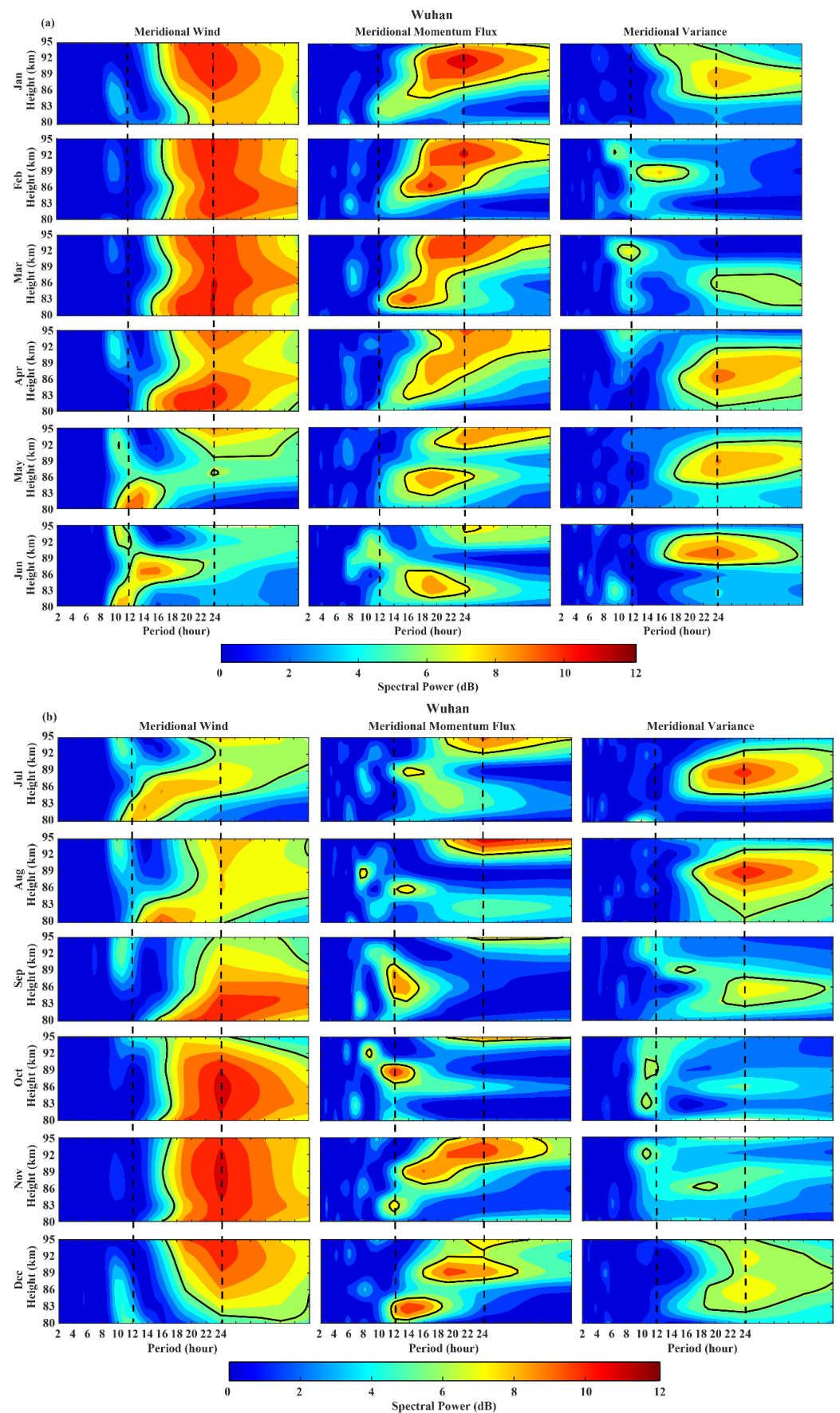


Figure 5. LS spectra of the background meridional wind (left column), meridional momentum flux

(middle column) and meridional variance (right column) using composite day analysis for 12 calendar months at Wuhan. The black solid lines indicate 95% confidence levels. (a) LS spectra from January to June; (b) LS spectra from July to December.

3.2. Seasonal Variation

Figure 6a presents the height/time cross-sections of the monthly averaged background zonal wind (left column), monthly averaged zonal momentum flux (middle column) and monthly averaged zonal variance (right column) at Mohe and Wuhan. It can be seen from the left column of Figure 6a that the monthly averaged zonal wind structures at Wuhan and Mohe are different. At Mohe, the zonal wind is westward at all heights ranges in April. In addition, a westward jet is observed below 86 km from May to July. There are two eastward jets at Mohe; one appears below 89 km during the time period from September to March, and another one occurs above 86 km in the period from April to September. At Wuhan, the monthly averaged background zonal wind is almost eastward, apart from a westward jet observed below 83 km during the period from March to May. We can see from the middle column of Figure 6a that the zonal momentum flux above 89 km at Mohe is westward, while the zonal momentum flux below 89 km is eastward. Note that the easterly zonal momentum flux decreases with altitude, and the westerly momentum flux increases with altitude. The momentum flux at Wuhan is different from that at Mohe, which is almost westward and reaches its westward maximum in March and October. As shown in the right column of Figure 6a, at both Mohe and Wuhan, monthly averaged zonal variance increases with the height, which is due to the amplitude of GW increases as atmospheric density decreases exponentially with height. The zonal variance at Wuhan is larger than that at Mohe.

Figure 6b presents the LS spectra of monthly averaged background zonal wind (left column), monthly averaged zonal momentum flux (middle column) and monthly averaged zonal variance (right column) over 96 consecutive composite days from the years 2012 to 2019 at Mohe and Wuhan. The black solid lines indicate 90% confidence levels. It can be seen from the left column of Figure 6b that the monthly averaged zonal wind shows annual and semiannual oscillations at both stations. In addition, a weak quasi-4-month oscillation occurs near 86 km at Wuhan. As shown in the middle column of Figure 6b, the zonal meridional flux at Mohe also presents an intense annual oscillation, and that at Wuhan shows annual and semiannual oscillations. From the right column of Figure 6b, we can find that the zonal variance at Mohe shows obvious annual and semiannual oscillations. In addition, a weak quasi-4-month oscillation is also observed in zonal variance at Mohe. At Wuhan, the zonal variance just presents a semiannual oscillation.

Figure 7a presents the height/time cross-sections of monthly averaged background meridional wind (left column), monthly averaged meridional momentum flux (middle column) and monthly averaged meridional variance (right column) at Mohe and Wuhan. It can be seen from the left column of Figure 6a that the monthly averaged background meridional wind structures at Wuhan and Mohe are also different. At Mohe, the meridional wind is southward in spring and summer and northward in autumn and winter above 89 km, while the meridional wind at Wuhan is almost southward in an entire composite year apart from a northward jet that occurs below 89 km in winter. As shown in the middle column of Figure 7a, the meridional momentum flux at Mohe is predominantly southward above 89 km and northward below 89 km during the time period from May to August. In addition, the meridional momentum flux reaches its both southward and northward maximums in the summer at Mohe. The meridional momentum flux at Wuhan presents three northward jets appearing at heights ranges from 83 to 92 km in March, above 92 km in August and at all heights regions in October. As shown in the right column of Figure 7a, the meridional variance at Wuhan and Mohe increases with the increase of height, apart from the time period from March to August at Mohe when the zonal variance centers at height ranges from 83 to 89 km. The zonal high-frequency GWs activity (zonal variance) is strongest in May at Mohe, while it is intense in March and August at Wuhan.

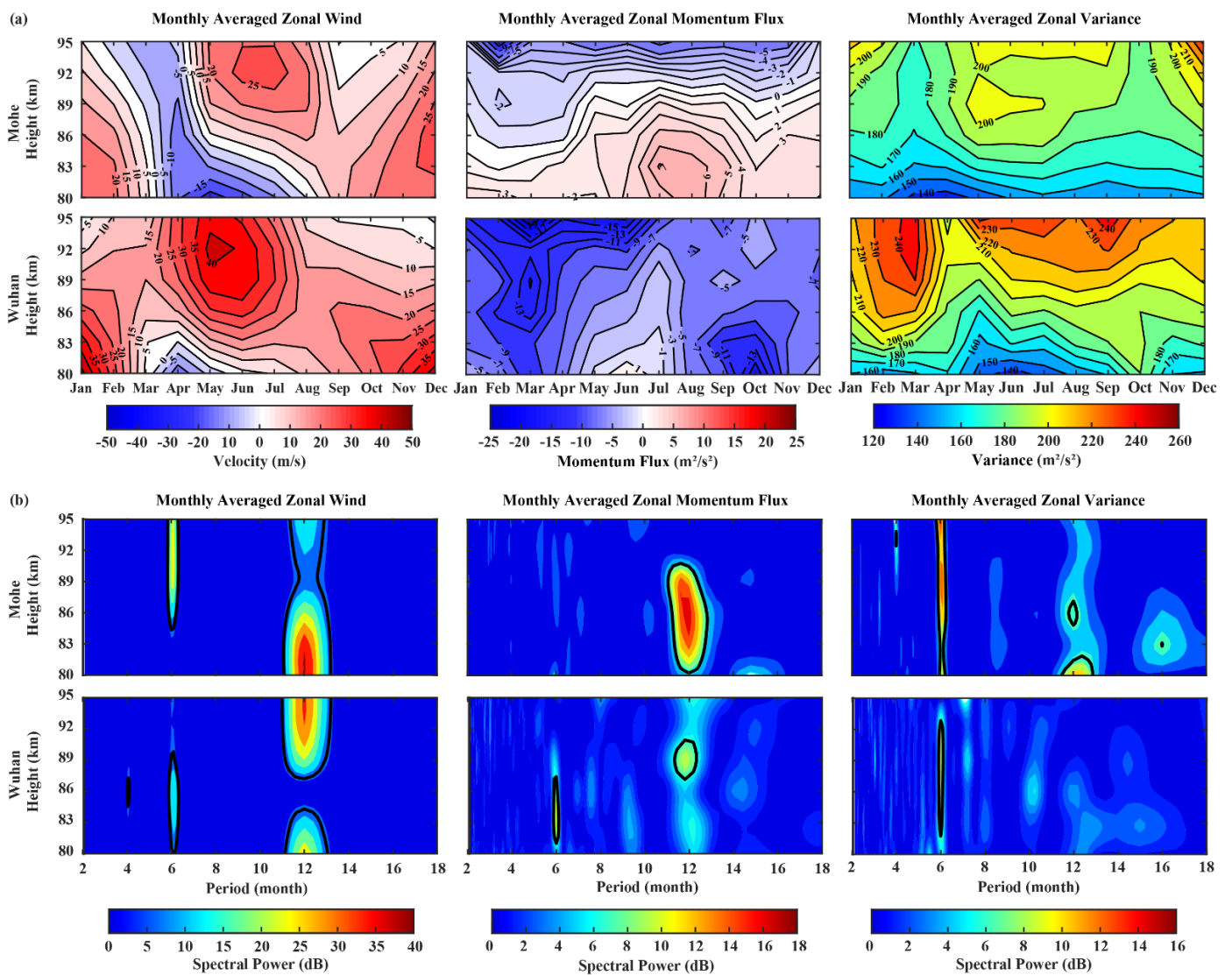


Figure 6. (a) Height/time cross-sections of monthly averaged background zonal wind (left column), monthly averaged zonal momentum flux (middle column) and monthly averaged zonal variance (right column) at Mohe and Wuhan. (b) LS spectra of the corresponding parameters in Figure 6a over 96 consecutive composite days from years 2012 to 2019. The black solid lines indicate 90% confidence levels.

Figure 7b presents the LS spectra of monthly averaged background meridional wind (left column), monthly averaged meridional momentum flux (middle column) and monthly averaged meridional variance (right column) over 96 consecutive composite days from the years 2012 to 2019 at Mohe and Wuhan. The black solid lines indicate 90% confidence levels. It can be seen from the left column of Figure 7b that the meridional wind at both stations shows a strong annual oscillation at all heights regions and a weak semiannual oscillation at a certain heights range with confidence intervals greater than 90%. We can see from the middle column of Figure 7b that the monthly averaged meridional momentum flux shows an intense annual oscillation at all heights ranges at Mohe. In addition, some very weak oscillations, such as quasi-4-month and 6-month, are observed near 89 km and below 83 km at Mohe. The monthly averaged meridional momentum flux at Wuhan just shows a weak semiannual oscillation at heights ranges from 83 to 89 km. As shown in the right column of Figure 7b, the meridional variance at Mohe presents an intense annual oscillation below 89 km, a semiannual oscillation at all heights ranges and a quasi-4-month oscillation above 89 km. At Wuhan, the meridional variance just shows a very weak semiannual oscillation.

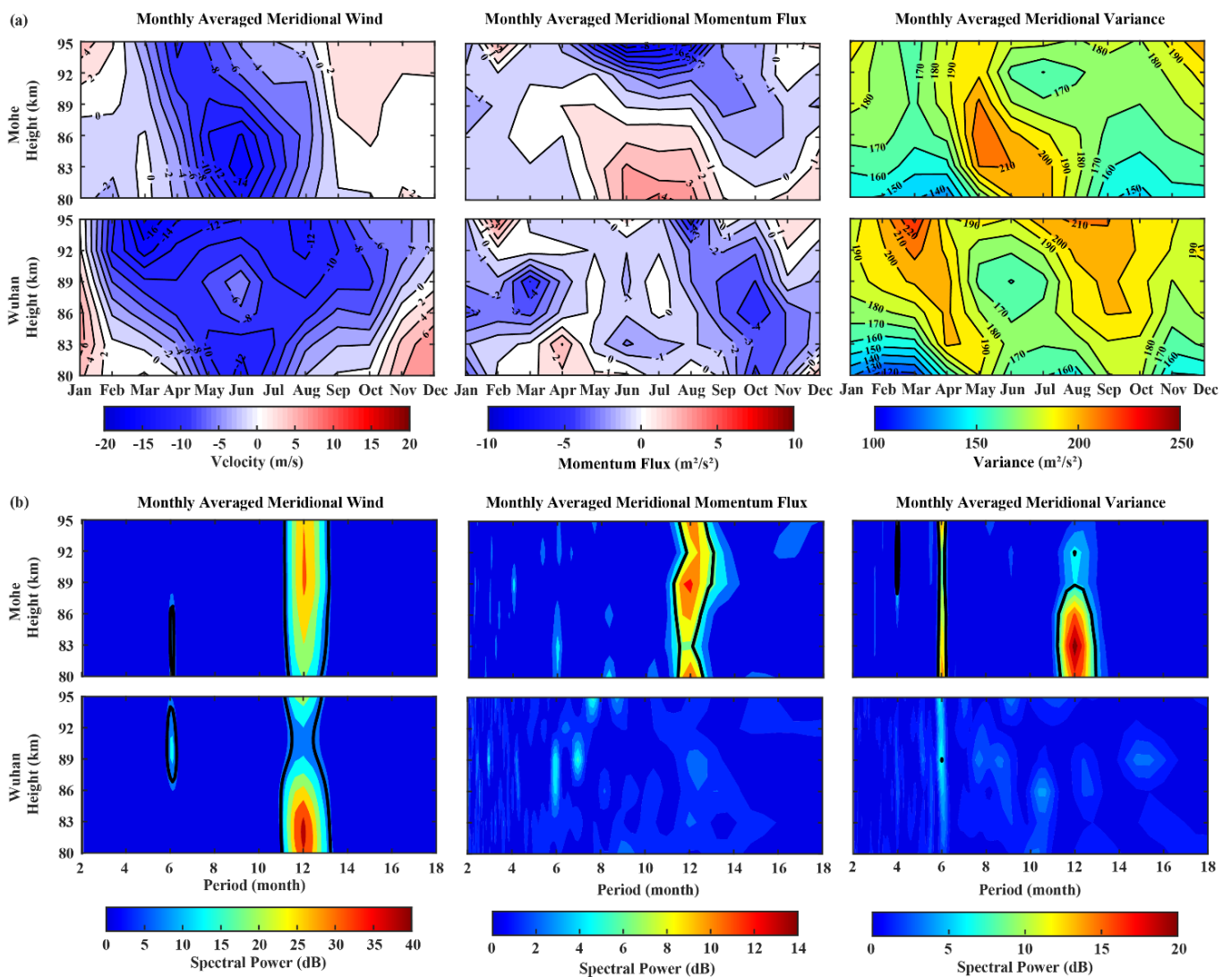


Figure 7. (a) Height/time cross-sections of monthly averaged background meridional wind (left column), monthly averaged meridional momentum flux (middle column) and monthly averaged meridional variance (right column) at Mohe and Wuhan. (b) LS spectra of the corresponding parameters in (a) over 96 consecutive composite days from years 2012 to 2019. The black solid lines indicate 90% confidence levels.

4. Discussion

The wind speeds associated with tides are similar to the phase speeds of GWs, which will promote interactions [14,29,30]. The interactions between the tides and GWs may have a great influence on the short-term variations of the semidiurnal tides at high latitudes [31]. In addition, the interactions between diurnal tides and GWs have also been observed at low and mid latitudes [32–34]. Walterscheid [35] suggested that the tidal winds represented an oscillating mean to the GWs, which modulated the accelerations of the mean flow to create the tidal variability. Beldon and Mitchell [28] proposed that the diurnal and semidiurnal tides had important modulation effects on GWs. Thayaparan et al. [33] proposed that tides (diurnal)/GWs interactions in the MLT region could occur at certain times of a year. Such interactions may be an important source for short-term tidal variability. As shown in Figures 2 and 3, both the zonal wind and the zonal momentum flux show an obvious 12 h (semidiurnal) periodicity at a certain heights range during the period from January to March and from September to December at Mohe and in June at Wuhan. In addition, both of them present intense 24 h (diurnal) periodicity in February, March and November at

Wuhan. Similarly, it can be seen from Figures 4 and 5 that both the meridional momentum flux and the meridional wind present a 12 h period during the time period from August to October at Mohe and 24 h period in the time periods of August, November and from January to May at Wuhan. The momentum flux and the background wind present the same periodicity at the same time, station and height, which indicates that the momentum flux of high-frequency GWs is modulated by the diurnal and semidiurnal tides. In addition to the momentum flux, the diurnal variation on the variance is also modulated by the tides. Thayaparan et al. [33] found a 24 h modulation on the variances in summer and winter over London, Canada (52° N), and concluded that GWs with periods less than 2 h can significantly modulate the tidal amplitudes, or conversely, GWs activity could be modulated by the tides. As shown in Figure 2, the zonal high-frequency GWs activity (zonal variance) presents 24 h periodicity at Mohe, while the dominant period in zonal wind is 12 h periodicity, which indicates that the tidal modulation on the zonal high-frequency GWs activity is weak. As presented in Figure 3, both the zonal wind and zonal variance present 24 h periodicity in January, February, March and October, indicating the diurnal tidal modulation on high-frequency GWs activity, which is consistent with the conclusion of Thayaparan et al. [33]. Similarly, the meridional wind and meridional variance at Mohe, as shown in Figure 4, also present the same 12 h periodicity in June, July and October. In addition, as shown in Figure 5, both of them at Wuhan present the same 24 h periodicity in January, April, May, August, September and December. It seems that the high-frequency GWs activity is strongly modulated by diurnal tides at Wuhan. Fritts et al. [32] studied the diurnal tidal modulation on GWs momentum flux during 3 days of large diurnal tidal winds and found the peak momentum flux was ~ 10 times as large as the mean momentum flux, indicating that the GWs momentum flux was greater during the intense diurnal tides. Thayaparan et al. [33], Isler et al. [36] and Manson et al. [14] also found significant peaks in GWs variances at the dominant tide periods. The previous studies have found that GWs momentum flux and variance are more intense near tidal harmonics, indicating the GWs activity is more intense near tidal harmonics, which is consistent with our conclusion (tidal modulation on GWs). In some months, weak 6 and 8 h periods are observed in the momentum flux and the variance, which may be caused by the high harmonic components of the tidal waves. However, the LS spectra of the background horizontal wind do not show significantly high harmonic components, which indicates that tidal modulation cannot fully explain this phenomenon.

The background wind has a filtering effect on GWs, which indicates that GWs with moderate phase velocity can propagate vertically when they move against the mean background wind. Otherwise, GWs will be filtered as they reach critical levels when the phase speeds of GWs approach the background wind speeds [3,37]. Based on the data of SKIYMET meteor radar at Trondheim, Norway (63.4° N, 10.5° E), de Wit et al. [38] studied the seasonal cycle of the momentum flux of GWs in the mesopause region and interpreted the seasonal cycle of the momentum flux of GWs as the selective filtering of a uniform spectrum of vertically propagating GWs between the surface and the mesopause region. It can be seen from Figure 6a that the zonal momentum flux shows an anti-correlated pattern to the zonal wind pattern at both stations, which demonstrates the coupling between the background wind and the momentum flux, or the filtering effect of wind on GWs. As shown in Figure 6b, both of the zonal momentum flux and zonal wind present the annual oscillation at both stations and semiannual oscillation at Wuhan, indicating the correlation between the background wind and high-frequency GWs activity. In addition, both the zonal background wind and the zonal variance show the annual oscillation at Mohe and semiannual oscillation at both stations. The annual and semiannual oscillations of the high-frequency GWs activity may be related to the annual and semiannual oscillations of the background wind, which is consistent with wind filtering. In addition, the quasi-4-month oscillation of the zonal variance is observed at Mohe, which may be the result of nonlinear interaction between the annual and semiannual oscillations. Similarly, as shown in Figure 7, the meridional momentum flux shows an anti-correlated pattern to the meridional wind

pattern at Mohe, so the seasonality of the meridional momentum flux at Mohe can also be explained by wind filtering. Thus, both the meridional momentum flux and meridional wind present an intense annual oscillation at Mohe. In addition, both the meridional background wind and meridional variance at Mohe show the annual and semiannual oscillations, which are consistent with wind filtering. The quasi-4-month oscillation of the meridional variance is also observed at Mohe. However, both the meridional momentum flux and the meridional wind are almost southward at Wuhan, so the seasonality of the meridional momentum flux at Wuhan cannot be explained by wind filtering. The secondary GWs with breaking mountain waves (MWs) in weak stratospheric winds over large terrains may easily attain large amplitudes and momentum fluxes above their source regions, and the momentum fluxes in these regions can propagate upward for great distances [39–42]. Zhao et al. [43] analyzed the data of the mobile Rayleigh Doppler lidars and found that the inertia gravity waves and MWs existed at the same time in the mid-latitude sites in China. Xinzhou (38.425° N, 112.729° E), one of the analysis sites of Zhao et al. [43], is close to Wuhan (30.5° N, 114.2° E). In addition, Wuhan is surrounded by the Dabie Mountains in the north. The southward propagation of the secondary GWs generated by the MWs and strong southerly wind filtering in the mesosphere may cause the abnormal situation in Wuhan. Hence, further research of MWs in Wuhan is needed. Due to the absence of the wind filtering, the meridional momentum flux only presents a weak semiannual oscillation. We can see from Figure 7a that the monthly averaged meridional variance at Wuhan presents an obvious semiannual oscillation, but the LS spectra of it for consecutive years, as shown in Figure 7b, do not present the intense semiannual oscillation. That may be due to the high-frequency GWs activity with semiannual oscillation being very intense during a period of consecutive years.

In this paper, the diurnal and seasonal variations of the momentum flux and variance in the MLT region were analyzed. According to the comparisons of different parameters of these two stations, we found that the high-frequency GWs activity shows a latitude dependence. As shown in Figures 2–5, the 12 h periodicity in the momentum flux at Mohe is stronger than the 24 h periodicity, which is consistent with the semidiurnal tidal modulation on background wind. The 24 h periodicity in the momentum flux at Wuhan is stronger than 12 h periodicity, which is also consistent with the dominant diurnal tidal modulation on background wind. At high latitudes, the interaction between semidiurnal tides and high-frequency GWs activity plays an important role, while at low and middle latitudes the interaction between diurnal tides and high-frequency GWs activity plays an important role, so the diurnal variation differences of the momentum flux may be caused by the different interactions of the high-frequency GWs activity and tidal waves between these two stations. The intensity of the variance represents the intensity of the high-frequency GWs activity. The modulation on the high-frequency GWs activity with a 24 h period is observed more frequently at both stations, which is consistent with the conclusion of Beldon and Mitchell [28]. As shown in Figures 6 and 7, the zonal momentum flux presents annual oscillation at both stations, and that at Wuhan also presents a semiannual oscillation. In addition, the meridional momentum flux at Mohe presents an intense annual oscillation, while that at Wuhan only presents a very weak semiannual oscillation. The latitudinal differences in the momentum flux of GWs could be caused by the different wind structures at low altitudes of these two stations, which have different filtering effects on surface wind velocity at different latitudes and the different sources of GWs, which may vary with latitudes. Gavrilov et al. [44] proposed that the seasonal differences in the variance of GWs may be attributed to the changes in the strengths of internal gravity wave (IGWs) sources at different altitudes and with the conditions of wave propagation in the atmosphere. It can be seen from Figures 6 and 7 that the high-frequency GWs activity (variance) presents the annual, semiannual and quasi-4-month oscillations at Mohe, while the high-frequency GWs activity presents semiannual oscillation at Wuhan. These seasonal differences in the high-frequency GWs activity could be caused by the changes in the strengths of IGW

sources at these two stations and with the different conditions of wave propagation in the atmosphere.

5. Summary

In this paper, we investigated diurnal and seasonal variations of high-frequency GWs activity at Mohe and Wuhan. Our main findings are summarized as follows:

1. The meridional momentum flux of GWs presents an anti-correlated pattern to the meridional wind pattern at Mohe, which is due to the wind filtering of GWs, while the meridional momentum flux is almost southward at Wuhan without the correlation with the background meridional wind.
2. The 24 h variation of the high-frequency GWs activity is observed more frequently at both stations.
3. The high-frequency GWs activity at Mohe shows obvious annual and semiannual oscillations, while that at Wuhan only presents a weak semiannual oscillation. In addition, a quasi-4-month oscillation is observed at Mohe.

Author Contributions: Methodology and investigation, Y.W. and Z.C.; data curation and writing—original draft preparation, Y.W.; writing—review and editing, Y.W., Q.T., Z.C., C.Z. and Y.L.; funding acquisition, C.Z. All authors have read and agreed to the published version of the manuscript.

Funding: This research was funded by the National Natural Science Foundation of China (NSFC grant no. 41574146 and 41774162), the National Key R&D Program of China (grant no. 2018YFC1503506) and the foundation of National Key Laboratory of Electromagnetic Environment (grant no. 6142403180204).

Institutional Review Board Statement: Not applicable.

Informed Consent Statement: Not applicable.

Data Availability Statement: The data of the Mohe and Wuhan stations are provided by the Chinese Meridian Project, which can be downloaded from <http://data.meridianproject.ac.cn> (accessed on 31 May 2022).

Acknowledgments: We acknowledge the use of a meteor radar dataset provided by the Chinese Meridian Project.

Conflicts of Interest: The authors declare no conflict of interest.

References

1. Placke, M. Gravity Waves and Momentum Fluxes in the Mesosphere and Lower Thermosphere Region. Master's Thesis, University of Rostock, Rostock, Germany, 2014.
2. Fritts, D.C.; Alexander, M.J. Gravity wave dynamics and effects in the middle atmosphere. *Rev. Geophys.* **2003**, *41*, 1003. [[CrossRef](#)]
3. Lindzen, R.S. Turbulence and stress owing to gravity wave and tidal breakdown. *J. Geophys. Res. Ocean.* **1981**, *86*, 9707–9714. [[CrossRef](#)]
4. Holton, J.R. The Role of Gravity Wave Induced Drag and Diffusion in the Momentum Budget of the Mesosphere. *J. Atmos. Sci.* **1982**, *39*, 791–799. [[CrossRef](#)]
5. Andrioli, V.F.; Batista, P.P.; Clemesha, B.R.; Schuch, N.J.; Buriti, R.A. Multi-year observations of gravity wave momentum fluxes at low and middle latitudes inferred by all-sky meteor radar. *Ann. Geophys.* **2015**, *33*, 1183–1193. [[CrossRef](#)]
6. Ern, M.; Preusse, P.; Gille, J.C.; Hepplewhite, C.L.; Mlynczak, M.G.; Russell, J.M.; Riese, M. Implications for atmospheric dynamics derived from global observations of gravity wave momentum flux in stratosphere and mesosphere. *J. Geophys. Res. Atmos.* **2011**, *116*, D19107. [[CrossRef](#)]
7. Hoffmann, P.; Jacobi, C.; Borries, C. Possible planetary wave coupling between the stratosphere and ionosphere by gravity wave modulation. *J. Atmos. Sol. Terr. Phys.* **2012**, *75*, 71–80. [[CrossRef](#)]
8. Holton, J.R.; Alexander, M.J. The role of waves in the transport circulation of the middle atmosphere. In *Atmospheric Science across the Stratopause*, 1st ed.; Siskind, D.E., Eckermann, S.D., Summers, M.E., Eds.; American Geophysical Union: Washington, DC, USA, 2000; Volume 123, pp. 21–35.
9. Manson, A.H.; Meek, C.E.; Luo, Y.; Hocking, W.K.; MacDougall, J.; Riggan, D.; Fritts, D.C.; Vincent, R.A. Modulation of gravity waves by planetary waves (2 and 16 d): Observations with the North American-Pacific MLT-MFR radar network. *J. Atmos. Sol. Terr. Phys.* **2003**, *65*, 85–104. [[CrossRef](#)]

10. Jacobi, C.; Gavrilov, M.N.; Kürschner, D.; Fröhlich, K. Gravity wave climatology and trends in the mesosphere/lower thermosphere region deduced from low-frequency drift measurements 1984–2003 (52.1° N, 13.2° E). *J. Atmos. Sol. Terr. Phys.* **2006**, *68*, 1913–1923. [[CrossRef](#)]
11. Matsumoto, N.; Shinbori, A.; Riggin, D.M.; Tsuda, T. Measurement of momentum flux using two meteor radars in Indonesia. *Ann. Geophys.* **2016**, *34*, 369–377. [[CrossRef](#)]
12. Placke, M.; Stober, G.; Jacobi, C. Gravity wave momentum fluxes in the MLT—Part I: Seasonal variation at Collm (51.3° N, 13.0° E). *J. Atmos. Sol. Terr. Phys.* **2011**, *73*, 904–910. [[CrossRef](#)]
13. Liu, A.Z.; Lu, X.; Franke, S.J. Diurnal variation of gravity wave momentum flux and its forcing on the diurnal tide. *J. Geophys. Res. Atmos.* **2013**, *118*, 1668–1678. [[CrossRef](#)]
14. Manson, A.H.; Meek, C.E.; Hall, G.E. Correlations of gravity waves and tides in the mesosphere over Saskatoon. *J. Atmos. Sol. Terr. Phys.* **1998**, *60*, 1089–1107. [[CrossRef](#)]
15. Beldon, C.L.; Mitchell, N.J. Gravity waves in the mesopause region observed by meteor radar, 2: Climatologies of gravity waves in the Antarctic and Arctic. *J. Atmos. Sol. Terr. Phys.* **2009**, *71*, 875–884. [[CrossRef](#)]
16. Jia, M.; Xue, X.; Gu, S.Y.; Chen, T.D.; Ning, B.Q.; Wu, J.F.; Zeng, X.Y.; Dou, X.K. Multiyear Observations of Gravity Wave Momentum Fluxes in the Midlatitude Mesosphere and Lower Thermosphere Region by Meteor Radar. *J. Geophys. Res. Space Phys.* **2018**, *123*, 5684–5703. [[CrossRef](#)]
17. Andrioli, V.F.; Fritts, D.C.; Batista, P.P.; Clemesha, B.R.; Janches, D. Diurnal variation in gravity wave activity at low and middle latitudes. *Ann. Geophys.* **2013**, *31*, 2123–2135. [[CrossRef](#)]
18. Rauthe, M.; Gerding, M.; Lubken, F.J. Seasonal changes in gravity wave activity measured by lidars at mid-latitudes. *Atmos. Chem. Phys. Discuss.* **2008**, *8*, 13741–13773. [[CrossRef](#)]
19. Rapp, M.; Strelnikov, B.; Müllemann, A.; Lübken, F.J.; Fritts, D.C. Turbulence measurements and implications for gravity wave dissipation during the MaCWAVE/MIDAS rocket program. *Geophys. Res. Lett.* **2004**, *31*, L24S07. [[CrossRef](#)]
20. Krebsbach, M.; Preusse, P. Spectral analysis of gravity wave activity in SABER temperature data. *Geophys. Res. Lett.* **2007**, *34*, L03814. [[CrossRef](#)]
21. Hocking, W.K.; Fuller, B.; Vandeppeer, B. Real-time determination of meteor-related parameters utilizing modern digital technology. *J. Atmos. Sol. Terr. Phys.* **2001**, *63*, 155–169. [[CrossRef](#)]
22. Holdsworth, D.A.; Reid, I.M.; Cervera, M.A. Buckland Park all-sky interferometric meteor radar. *Radio. Sci.* **2004**, *39*, RS5009. [[CrossRef](#)]
23. Reid, J.D.; Choi, C.H.; Oldroyd, N.O. Calcium oxalate crystals in the thyroid: Their identification, prevalence, origin, and possible significance. *Am. J. Clin. Pathol.* **1987**, *87*, 443–454. [[CrossRef](#)]
24. Hocking, W.K. A new approach to momentum flux determinations using SKiYMET meteor radars. *Ann. Geophys.* **2005**, *23*, 2433–2439. [[CrossRef](#)]
25. Vincent, R.A.; Kovalam, S.; Reid, I.M.; Younger, J.P. Gravity wave flux retrievals using meteor radars. *Geophys. Res. Lett.* **2010**, *37*, L14802. [[CrossRef](#)]
26. de Wit, R.J.; Hibbins, R.E.; Espy, P.J.; Orsolini, Y.J.; Limpasuvan, V.; Kinnison, D.E. Observations of gravity wave forcing of the mesopause region during the January 2013 major Sudden Stratospheric Warming. *Geophys. Res. Lett.* **2014**, *41*, 4745–4752. [[CrossRef](#)]
27. Spargo, A.J.; Reid, I.M.; Mackinnon, A.D. Multistatic meteor radar observations of gravity-wave–tidal interaction over southern Australia. *Atmos. Meas. Tech.* **2019**, *12*, 4791–4812. [[CrossRef](#)]
28. Beldon, C.L.; Mitchell, N.J. Gravity wave–tidal interactions in the mesosphere and lower thermosphere over Rothera, Antarctica (68° S, 68° W). *J. Geophys. Res. Atmos.* **2010**, *115*, D18101. [[CrossRef](#)]
29. Espy, P.J. Tidal modulation of the gravity-wave momentum flux in the Antarctic mesosphere. *Geophys. Res. Lett.* **2004**, *31*, L11111. [[CrossRef](#)]
30. Hall, C.M.; Nozawa, S.; Manson, A.H.; Meek, C.E. Tidal signatures in mesospheric turbulence. *Ann. Geophys.* **2006**, *24*, 453–465. [[CrossRef](#)]
31. Charles, K.; Jones, G. Mesospheric mean winds and tides observed by the imaging Doppler interferometer (IDI) at Halley, Antarctica. *J. Atmos. Sol. Terr. Phys.* **1999**, *61*, 351–362. [[CrossRef](#)]
32. Fritts, D.C.; Vincent, R.A. Mesospheric momentum flux studies at Adelaide, Australia: Observations and a gravity wave-tidal interaction model. *J. Atmos. Sci.* **1987**, *44*, 605–619. [[CrossRef](#)]
33. Thayaparan, T.; Hocking, W.K.; MacDougall, J. Observational evidence of tidal/gravity wave interactions using the UWO 2MHz radar. *Geophys. Res. Lett.* **1995**, *22*, 373–376. [[CrossRef](#)]
34. Nakamura, T.; Fritts, D.C.; Isler, J.R.; Tsuda, T.; Vincent, R.A.; Reid, I.M. Short-period fluctuations of the diurnal tide observed with low-latitude MF and meteor radars during CADRE: Evidence for gravity wave/tidal interactions. *J. Geophys. Res.* **1997**, *102*, 26225–26238. [[CrossRef](#)]
35. Walterscheid, R.L. Inertio-gravity wave induced accelerations of mean flow having an imposed periodic component: Implications for tidal observations in the meteor region. *J. Geophys. Res.* **1981**, *86*, 9698–9706. [[CrossRef](#)]
36. Isler, J.R.; Fritts, D.C. Gravity wave variability and interaction with lower-frequency motions in the mesosphere and lower thermosphere over Hawaii. *J. Atmos. Sci.* **1996**, *53*, 37–48. [[CrossRef](#)]

37. Placke, M.; Hoffmann, P.; Latteck, R.; Rapp, M. Gravity wave momentum fluxes from MF and meteor radar measurements in the polar MLT region. *J. Geophys. Res. Space* **2015**, *120*, 736–750. [[CrossRef](#)]
38. de Wit, R.; Hibbins, R.; Espy, P.J. The seasonal cycle of gravity wave momentum flux and forcing in the high latitude northern hemisphere mesopause region. *J. Atmos. Sol. Terr. Phys.* **2015**, *127*, 21–29. [[CrossRef](#)]
39. Lilly, D.K. Stratified turbulence and the mesoscale variability of the atmosphere. *J. Atmos. Sci.* **1983**, *40*, 749–761. [[CrossRef](#)]
40. Satomura, T.; Sato, K. Secondary generation of gravity waves associated with the breaking of mountain waves. *J. Atmos. Sci.* **1999**, *56*, 3847–3858. [[CrossRef](#)]
41. Smith, R.B.; Woods, B.K.; Jensen, J.; Cooper, W.A.; Doyle, J.D.; Jiang, Q.; Grubisic, V. Mountain waves entering the stratosphere. *J. Atmos. Sci.* **2008**, *65*, 2543–2562. [[CrossRef](#)]
42. Wit, R.D.; Janches, D.; Fritts, D.C.; Stockwell, R.G.; Coy, L. Unexpected climatological behavior of MLT gravity wave momentum flux in the lee of the Southern Andes hot spot. *Geophys. Res. Lett.* **2017**, *44*, 1182–1191. [[CrossRef](#)]
43. Zhao, R.; Dou, X.; Xue, X.; Sun, D.; Han, Y.; Chen, C.; Zheng, J.; Li, Z.; Zhou, A.; Han, Y.; et al. Stratosphere and lower mesosphere wind observation and gravity wave activities of the wind field in China using a mobile Rayleigh Doppler lidar. *J. Geophys. Res. Space* **2017**, *122*, 8847–8857. [[CrossRef](#)]
44. Gavrilov, N.M.; Fukao, S.; Nakamura, T.; Jacobi, C.; Kürschner, D.; Manson, A.H.; Meek, C.E. Comparative study of interannual changes of the mean winds and gravity wave activity in the middle atmosphere over Japan, Central Europe and Canada. *J. Atmos. Sol. Terr. Phys.* **2002**, *64*, 1003–1010. [[CrossRef](#)]